Hindawi
Journal of Nanomaterials
Volume 2018, Article ID 9651039, 10 pages
https://doi.org/10.1155/2018/9651039

Research Article

Synthesis and Characterization of Ti-Fe Oxide Nanomaterials for Lead Removal

Buzuayehu Abebe and H. C. Ananda Murthy

Department of Applied Chemistry, School of Applied Natural Sciences, Adama Science and Technology University, P.O. Box 1888, Adama, Ethiopia

Correspondence should be addressed to Buzuayehu Abebe; buzea8@gmail.com

Received 25 May 2018; Revised 16 August 2018; Accepted 9 September 2018; Published 7 November 2018

Guest Editor: Maria Giulia Faga

TiO_2-Fe_2O_3 binary oxides containing different percentage of Fe_2O_3 were synthesized using impregnation method. The Fourier transform infrared spectroscopy (FT-IR), X-ray diffraction (XRD), scanning electron microscopy with energy-dispersive X-ray spectroscopy (SEM-EDX), and thermogravimetric with differential thermal analyzer (TG-DTA) analytical techniques were used for understanding of the physicochemical properties and well impregnation of Fe_2O_3 in TiO_2 lattice. During adsorption study, pH of the solution, adsorbent dosage, time of contact, agitation speed, and concentration of adsorbate were optimized. From Langmuir, Freundlich, FG, D-RK, Temkin, and FH adsorption isotherm models, relatively, Langmuir isotherm model fits well. For adsorption-reaction kinetic model, pseudo-first order (PFO), pseudo-second order (PSO), and Elovich were tested and intraparticle diffusion (IPD) for adsorption-diffusion kinetic models. Out of those, the PSO fits well; this indicates that the mechanism of adsorption is under control of adsorption-reaction. The mean adsorption energy, spontaneity, and reproducibility of the adsorbent were also conducted, and all of those studies support the domination of physical adsorption mechanism.

1. Introduction

Heavy metals are toxic pollutants which are not degradable biologically. The consumption of those heavy metals, even at trace level, has a risk for human beings. Therefore, removing of those metals is important [1]. Materials in nanosize range exhibit distinct properties and effective process parameters for removing pollutants. This is because of the small particle size (high surface area to volume ratio), specificity for pollutants, magnetic separation properties, surface chemistry, and surface interactions. In recent years, the use of semiconductor metal oxides for the removal of pollutants has gained more attention in the scientific community. Those oxide nanoparticles have been widely studied due to their new optical, magnetic, electronic, thermal, and mechanical behaviors and their roles in pollutant removal, catalyst, gas sensors, and photoelectronic device applications [2].

Liquid-solid translation synthesis methods of metal oxide nanomaterial are largely used in order to regulate the shape, size, and structural features of the nanomaterials. Among many synthesis routes, frequently applied methods are sol-gel [3], coprecipitation [4], micelle and inverse micelle [5], hydrothermal method [6], mesoporous/nanoporous [7], sonochemical [8], and impregnation [9, 10]. The most common techniques used for heavy metal treatment include reduction and precipitation [11], coagulation-flocculation [12], electrocoagulation [13], adsorption [14], and membrane and ultramembrane filtration [15]. Among those different techniques, adsorption is the most common and popular method used to reduce pollutants that enter into water bodies.

Current studies have confirmed that nanosized titanium oxide has a number of unique properties (e.g., it is cheap, has high surface area, highly porous, nontoxic, high degree of contact, and hydrophilic in nature). It is also the most appropriate semiconductor for remediation of heavy metals and degradation of different dyes from aqueous solution. Even if this metal oxide has several positive key properties related to removal of pollutants, the agglomeration between its particles is the main problem. To overcome this challenge,

which makes it useless for pollutant remediation after, many researchers had tried in the past to develop TiO_2-based mixed oxide materials that can give large number of adsorptive sites without agglomeration. Among different types of metal oxides, iron oxide is found to be the best choice. And the most common iron oxides are γ-Fe_2O_3, α-Fe_2O_3, and Fe_3O_4 [4].

In this study, Ti-Fe binary oxides were synthesized by impregnation of iron oxide into titanium oxide using impregnation method. The *as*-synthesized material was characterized by TG-DTA (DTG-60H), FT-IR (Bruker IFS120 M PerkinElmer), and XRD and SEM/EDXS (ZEISS EVO 18) analytical techniques. And its adsorption capacity has been tested by removing the lead ion from aqueous solution. The explanation of adsorption isotherms about homogeneity, heterogeneity, fractional coverage, mean adsorption energy, energy of adsorbate-adsorbate interaction, and spontaneity was tested by Langmuir, Freundlich, FG, D-RK, Temkin, FH models, respectively. For adsorption-reaction kinetic study, PFO, PSO, and Elovich models were used, and for adsorption-diffusion kinetic studies, the IPD model was used. The effect of temperature and desorption experiments were also done.

2. Methodology

2.1. Synthesis. Impregnation method was used to synthesize nanosized TiO_2-Fe_2O_3 binary oxides [9, 10]. To prepare a 0.1 M solution, initially, iron (III) nitrate nonahydrate [$(Fe(NO_3)_3{\cdot}9H_2O]$ (99.95%) as precursor salt was dissolved in deionized water, and in this solution, the powder TiO_2 was added. The temperature of the solution was adjusted to 80°C on hotplate with constant stirring magnetic stirrer. Dilute NaOH was added dropwise to increase the pH of the solution from 3 to 8 and aged with stirring continuously for one hour for oxidation of Fe_3O_4 to Fe_2O_3. The precipitate was centrifuged and washed repeatedly with alcohol and water. Finally, it was calcined for 2 hours at 450°C after drying it in an oven at 110°C overnight. All chemicals/reagents used for this study have analytical grade purity.

2.2. Batch Adsorption Experiments. The adsorption experiment was carried out in 50 mL Erlenmeyer flasks having Ti-Fe oxide to lead ion aqueous solution ratio of 1 : 300 [0.1 g of iron oxides: 30 mL of 35 mg/L of Pb $(NO_3)_3$]. Equilibration of the experiments was done on a rotary shaker. Then, the obtained solution was filtered to separate the residue from the solution. The amount of lead ion deposited on adsorbent was obtained with the help of atomic adsorption spectroscopy (AAS). During the sorption experiments, the pH of the solution, dosage, speed of agitation, time of contact, and initial lead ion concentration were optimized. From the mass balance for the adsorbate in the glassware, the equation becomes

$$m(q_o - q_e) = (C_o - C_e)v. \quad (1)$$

To determine the equilibrium relationship at $q_o = 0$, the relation becomes

$$q_e = \frac{v}{m} \times (C_o - C_e). \quad (2)$$

The percent of sorption (%) was calculated using equation

$$\% = \left(\frac{C_o - C_e}{C_o}\right) * 100, \quad (3)$$

where C_o is the initial concentration (mg/L) and C_e is the equilibrium concentration (mg/L) of lead ion, q_e is the adsorption capacity of adsorbent (mg/g), v is the volume of reaction mixture (L), and m is the mass of adsorbent used (g).

2.2.1. Optimization of Parameters. To optimize the effect of pH on lead ion sorption, 0.1 g of the sorbent was taken into 50 mL of Erlenmeyer flask containing 30 mL of 40 mg/L lead ions and varying the pH of the solutions as 2, 4, 6, 8, 10, and 12. To optimize the amounts of loaded powder, 0.05, 0.10, 0.15, 0.20, 0.25, 0.30, and 0.35 g of sorbent were taken. The effect of speed of agitation was optimized by adjusting the speed of the shaker as 40, 70, 100, 130, 160, and 190 rpm. During optimization, the first optimized parameters are kept at the optimized value and those that are not optimized are kept at constant value.

2.2.2. Adsorption Isotherms. Sorption isotherm experiment was done by taking all the optimized values of parameters and varying the lead ion concentration as 15, 25, 35, 45, 55, 65, and 75 mg/L in a separate 50 mL Erlenmeyer flask.

2.2.3. Kinetics of Sorption. The study of kinetics was conducted by taking various contact time (10, 40, 70, 100, 130, and 160 min), and all the optimized values of parameters were used.

2.3. Temperature Effect. In order to determine the effect of temperature on sorption phenomenon, all predetermined and optimized values of parameters were used and the temperature was established at 25, 35, 45, and 55°C.

2.4. Desorption Study. Reproducibility study was done using lead ion-loaded powder obtained after sorption experiment and using optimized values. 0.1 g of lead ion-loaded binary oxide powder was added into six 50 mL of Erlenmeyer flasks having approximately 30 mL of distilled water, and the pH of the solution was adjusted to 2, 4, 6, 8, 10, and 12 using acid and base.

3. Result and Discussions

3.1. XRD. Figure 1(a) shows the XRD diffraction spectra of TiO_2, TiO_2-Fe_2O_3, and Fe_2O_3. The sharpness of the peak on TiO_2 and TiO_2-Fe_2O_3 shows its crystallinity. The particle size was calculated using Debye-Scherrer equation, $D = K\lambda/\beta \cos\theta$, where d is the mean size, K is a constant (0.9), λ is the wavelength of X-ray (0.15506 nm), β is the line of broadening (in radian), and θ is the Bragg angle; $\beta = G - g$, where G is the line width (in radians) and g is the instrument line broadening (in radians) [16]. Among the various percentages of Fe_2O_3 impregnated into TiO_2 lattice, the optimized particle size value was

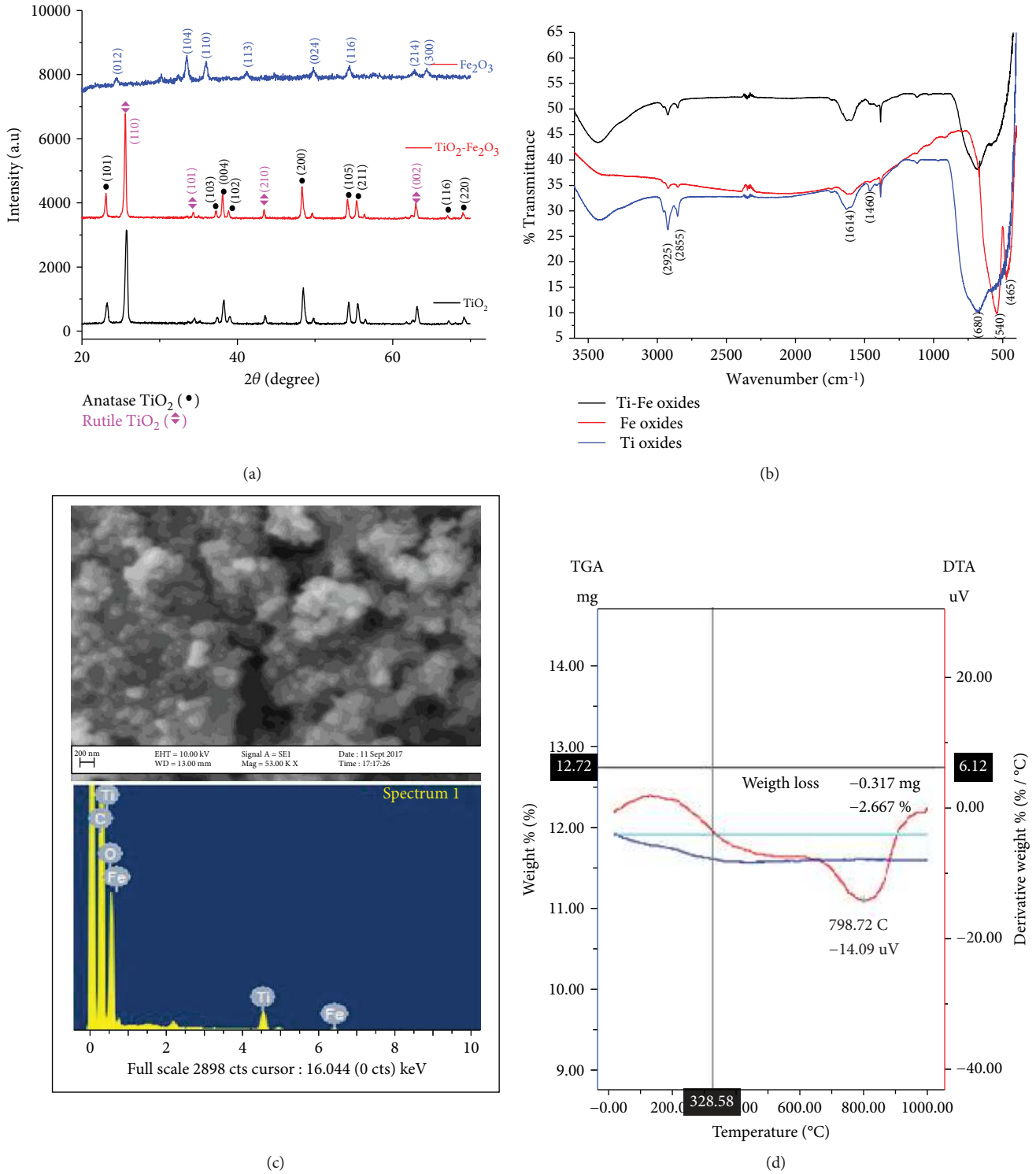

Figure 1: (a) XRD. (b) FT-IR. (c) SEM-EDX (TiO_2-Fe_2O_3). (d) TG-DTA spectra of nanosized metal oxides.

approximately found to be 31 nm (Table 1). The effects of Fe_2O_3 loading were investigated as shown in Table 1. The outcome revealed that the increase in loading of Fe_2O_3 causes increase in the particle size and then it further decreases as the percentage of iron oxide increases to 8.

In comparison with the separate titanium oxide peak and the reported result of pure titania spectra, 2θ corresponding to 23.5(101), 37.1(103), 38.2(004), 38.8(102), 48.4(200), 54.40(105), 55.5(211), 67.1(116), and 69.1(220) was for anatase and the other 26.0(110), 34.2(101), 43.4(210), and 63.2 (002) are for rutile [17, 18]. No matching iron oxide peaks appeared in TiO_2-Fe_2O_3 diffraction spectrum. This indicates the total impregnation of small percentage of iron oxide in the

Table 1: Description of percentage composition and XRD results of the *as*-synthesized powders.

TiO_2 (%)	Fe_2O_3 (%)	2θ (degree)	β (degree)	θ (radian)	D (nm)
100	0	25.713	0.3542	0.2244	24.05
96	4	25.567	0.2509	0.2237	33.93
92	8	25.598	0.2758	0.2240	30.87
88	12	25.607	0.2520	0.2241	33.79
0	100	33.476	0.5237	0.2921	16.56

lattice of titanium oxides. As suggested by Jamalluddin and Abdullah [19], the absence of appearance of peaks for Fe_2O_3 may be due to the close similarities in radii of titanium and iron ion which were 0.68 and 0.64 Å, respectively; these similarities may cause substitution of one ion by the other. The other reason for the absence of iron peak may be due to its small percentage relative to titanium oxides [20].

3.2. FT-IR. From FT-IR spectra (Figure 1(b)), the band appeared at 680 cm^{-1} was due to bending vibration of Ti-O and the broadband stretched from 500–700 cm^{-1} was due to Ti-O-Ti and Ti-O bending vibration, and on the pure iron oxide FR-IR spectra, the two sharp band appeared at 540(α -Fe_2O_3) and 465(γ-Fe_2O_3) was due to bending vibrations of Fe-O bond. Except for some small shifts and decreasing of bands on the spectra of TiO_2-Fe_2O_3, both TiO_2 and TiO_2-Fe_2O_3 spectra are almost similar; this indicates the well impregnation of Fe_2O_3 in TiO_2 lattice. In fact, the linking of those two oxides was well confirmed by SEM-EDX analysis. The broad and strong absorption band appeared around 3426 cm^{-1} and medium band at 1613 cm^{-1} are attributed to the stretching vibration of hydroxyl (O-H) and water (H-O-H) groups absorbed on the adsorbent surface, respectively. Those bands are common on metal oxides and very essential for adsorption process [21, 22].

3.3. SEM-EDX. From the SEM-EDX spectrum of Ti-Fe oxide (Figure 1(c)), a spherical shape of nearly equal size was observed. The EDXS spectrum confirms only the presence of Fe, Ti, C, and O. The appearance of carbon (C) is from the standard used during analysis. The appearance of only the three elements without any other elements indicates the purity of the powder.

3.4. TG-DTA. From TG-DTA graph (Figure 1(d)) initially due to the removal of the surface deposited moisture or solvent molecules on the powder, a little weight loss was observed in between 0 and 110°C. The other weight loss occurred in between 200 and 250°C is probably due to the breakdown of metal hydroxide bonds of $Fe(OH)_2$. Out of 11.886 mg total weight, the loss is only 0.317 mg (2.667%). Above the temperature of 380°C, no weight loss occurred; this indicates that the thermal stability of the metal oxides is quite stable up to 1000°C [23]. In fact, oxides may undergo phase transitions which are not simply seen by TGA.

3.5. Parameter Optimization. The effects of solution pH, dose, agitation speed, and time of contact for sorption of lead ion were conducted (Figure 2). During pH optimization, the greatest sorption was observed under alkaline pH range (Figure 2(a)). Due to H^+, the acidic pH makes the surface of metal oxides to be more positive, so repulsive interaction exists between the iron oxides and lead cation. Above seven pH value, the presence of OH^- assists the surface to be more negatively charged; therefore, the interactions become attractive [24]. On dosage optimization (Figure 2(b)), up to optimum point (0.1 g), the sorption efficiency was found to be high which is due to the availabilities of high sorption sites [25]. But, further increasing adsorbent dosage, it does not shows significant change, because the total number of the adsorbate becomes negligible. From Figure 2(c), as the speed of agitation increases, diffusion of lead ion towards the adsorbent surface also increases. After the optima (100 rpm), as the rate of agitation speed further increases, the adsorbate starts to desorb from the surface. And on contact time optimization (Figure 2(d)), after reaching optimum point 130 min, sorption capacity becomes constant since the sorbent sites were almost occupied.

3.6. Adsorption Isotherms. The experimental data conducted by taking different initial concentrations (Figure 2(e)) were fitted by Langmuir, Freundlich, Fowler-Guggenheim (FG), Flory-Huggins (FH), Temkin, and Dubinin-Radushkevich (D-RK) isotherm models. The linear equations for all isotherm models are given as follows:

$$\begin{aligned}
\text{Langmuir}: \left(\frac{C_o}{q_e}\right) &= \frac{1}{bq_{\max}} + \frac{C_e}{q_{\max}},\\
R_L &= \frac{1}{(1 + bC_{\mathrm{o}})},\\
\text{Freundlich}: \log q_e &= \log k_f + \left(\frac{1}{n}\right) \log C_e,\\
\text{Fowler-Guggenheim}: \frac{C_e(1-\theta)}{\theta} &= \left(\frac{2w}{RT}\right)\theta - \ln k_{\mathrm{FG}},\\
\text{Dubinin-Radushkevich}: \ln q_e &= \ln q_s - \beta\varepsilon^2,\\
\varepsilon &= RT \ln\left(1 + \frac{1}{C_e}\right),\\
E &= \frac{1}{\sqrt{2\beta}},\\
\text{Temkin}: q_e &= \left(\frac{RT}{b}\right) \ln k_T + \left(\frac{RT}{b}\right) \ln C_e,\\
\text{Flory-Huggins}: \ln\left(\frac{\theta}{C_o}\right) &= \ln k_{\mathrm{FH}} + n \ln(1-\theta),\\
\Delta G^o &= -RT \ln(k_{\mathrm{FH}}),
\end{aligned} \tag{4}$$

where C_o is the initial lead ion (adsorbate) concentration in solution (mg/L), C_e is the adsorbate equilibrium

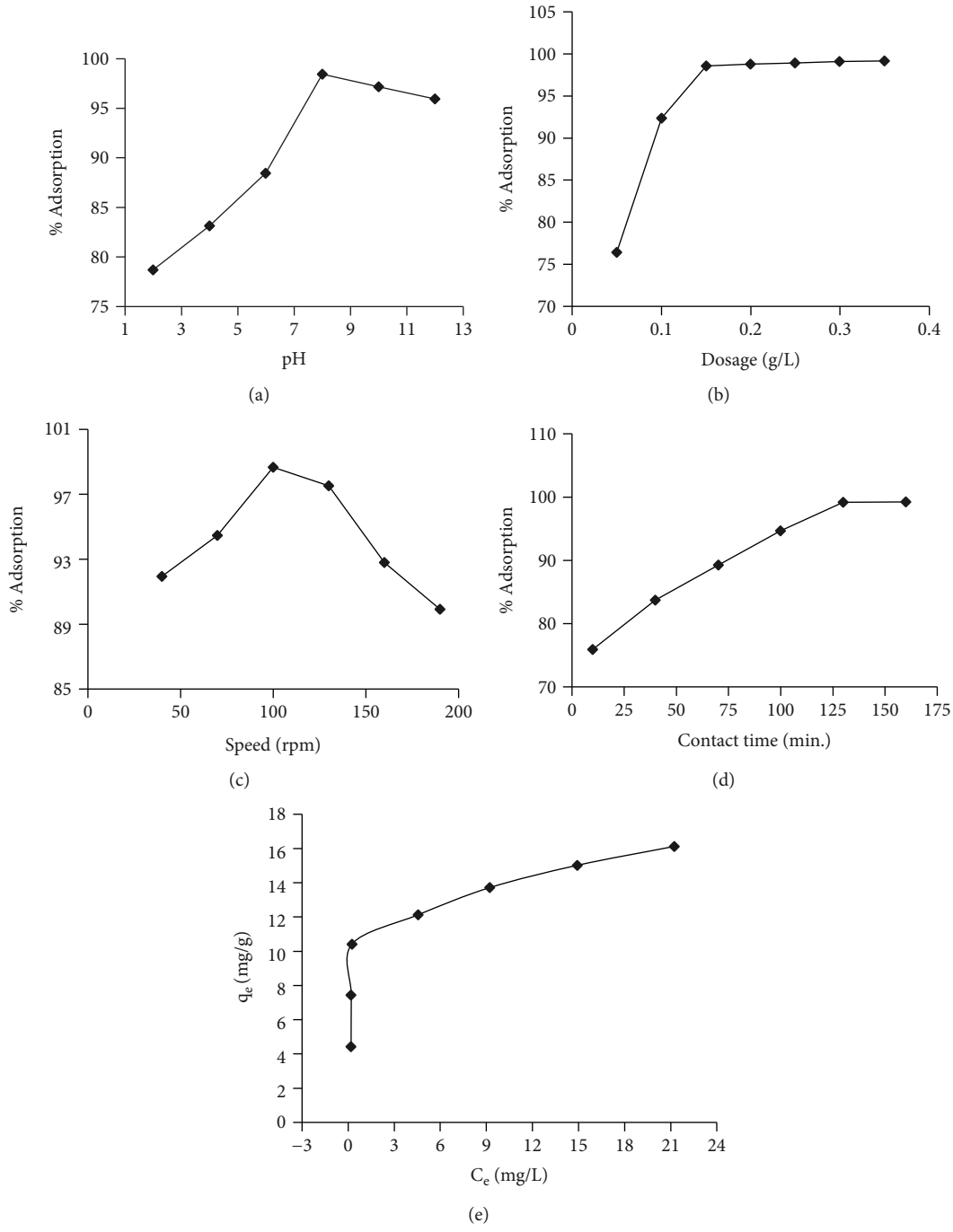

FIGURE 2: Effect of (a) pH, (b) adsorbent dose, (c) agitation speed, (d) contact time, and (e) adsorption isotherm for lead ion adsorption onto Ti-Fe oxide.

concentration in solution, q_e is the amount of adsorbate accumulated per gram of the adsorbent, $q_{\max}$ is the maximum uptake corresponding to the site saturation, b is the ratio of adsorption and desorption rates, k_f is the distribution coefficient and represents the quantity of adsorbate adsorbed onto adsorbent for unit equilibrium concentration, $1/n$ is an empirical constant related to the magnitude of the adsorption or surface heterogeneity, $\theta = [1 - (C_e/C_o)]$ is the fractional coverage, w is the interaction energy, ε is the Dubinin-Radushkevich isotherm constant, q_s is the saturation capacity (mg/g), β is the constant related to free energy, k_T is the Temkin isotherm equilibrium binding constant (L/g), b is the Temkin adsorption constant (J/molK), n is the number of ions occupying adsorption sites, T is the absolute temperature (k), and R is the universal gas constant (8.314 J/molK).

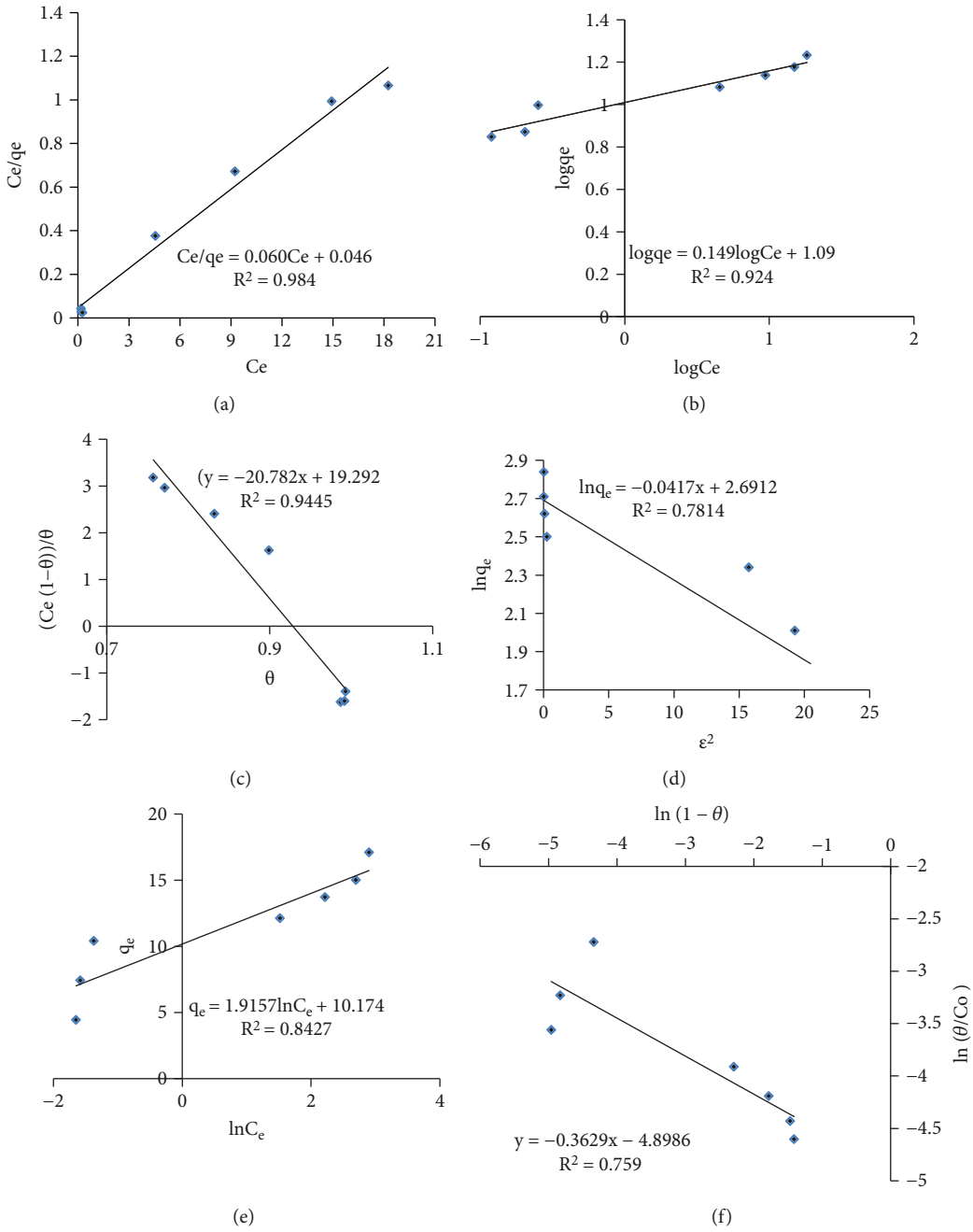

Figure 3: (a) Langmuir, (b) Freundlich, (c) Fowler-Guggenheim, (d) Dubinin-Radushkevich, (e) Temkin, and (f) Flory-Huggins adsorption isotherm.

Table 2: Kinetic constants for sorption of lead ion on binary oxide.

	Langmuir		Freundlich		Fowler-Guggenheim		Dubinin-Radushkevich		Temkin		Flory-Huggins	
q_{max}	b	R_L	k_f	n	k_{FG}	w (kJ/mol)	E (kJ/mol)	β	b (J/mol)	k_T	n	ΔG (kJ/mol)
16.67	1.3	0.02	10.21	6.71	$4.2 * s10^{-9}$	−25.7	3.45	−0.042	1293	202.5	−0.363	−12.137

Figures 3(a)–3(f) explain the sorption isothermal behavior based on concentration optimization results. The extracted sorption constant values are given in Table 2. Depending on R^2 values (given on each graph), Langmuir sorption isotherm model (Figure 3(a)) fits the sorption data relatively better than other models. The R_L value tells the type of isotherm to be unfavorable ($R_L > 1$), linear (=1), irreversible (=0), and favorable (<1).

The R_L values in this study were in between 0 and 1 indicating that the adsorption is favorable. The Freundlich isotherm model (Figure 3(b)), which is responsible for the heterogeneity of the adsorbent sites. Generally, if the value of constant n is in between 1 and 10, the adsorption process becomes acceptable; when the value of n is greater than one, physical adsorption process occurs; and if it is less than one, the adsorption process becomes chemically driven. The value of n obtained for this study was 6.71, which shows the domination of physical adsorption process and also indicates the presence of high affinity between adsorbate and absorbent.

From FG (Figure 3(c)) model which accounts the surface characteristics of adsorbate adsorbed on adsorbent, the value of heat of adsorption (w) being negative (−25.7 kJ/mol) indicates the presence of repulsive interaction between adsorbed molecules. D-RK (Figure 3(d)) and FH (Figure 3(e)) models fit relatively less; this may be because those models are suitable for only intermediate adsorbate concentration range. In D-RK isotherm model, the mean free energy, $E < 8$ kJ/mol, indicates the domination of physical adsorption, 8–16 kJ/mol (ion exchange) and 20–40 kJ/mol (chemical adsorption). The obtained mean free energy, E value for this study, was 3.45 kJ/mol, and this indicates that the physical adsorption is the controlling mechanism. The Temkin model (Figure 3(e)) is valid only for an intermediate range of adsorbate concentrations and gives information for adsorbate/adsorbate interactions. The constant k_T (202.5 L/g) on Temkin is an equilibrium binding constant which is related to maximum bonding energy. The FH model (Figure 3(f)) is responsible for the characteristic surface coverage of the adsorbate adsorbed on the adsorbent and responsible for suggesting the spontaneity of the reaction. The obtained value of standard free energy (ΔG^o) from FH model was −12.14 kJ/mol; this value indicates that the reaction was spontaneous. The obtained maximum uptake corresponding to the site saturation ($q_{\max}$) for the adsorbent is 16.67 mg/g.

3.7. Kinetics of Adsorption. To interpret time-dependent experimental data, the linear equations of the PFO, PSO, Elovich, and IPD were given as follows:

$$\begin{aligned}
&\text{Pseudo-first order} : \log\left(q_e - q_t\right) = -\left(\frac{K_1}{2.303}\right)t + \log q_e,\\
&\text{Pseudo-second order} : \frac{t}{q_t} = \left(\frac{1}{q_e}\right)t + \frac{1}{K_2 q_e^2},\\
&\text{Elovich} : q_t = \left(\frac{1}{\beta}\right)\ln\left(\alpha\beta\right) + \left(\frac{1}{\beta}\right)\ln t,\\
&\text{Weber-Morris IPD model} : q_t = k_i\sqrt{t} + C,
\end{aligned} \tag{5}$$

where q_e and q_t are the amounts of adsorbate adsorbed on the adsorbent at equilibrium and at various times, t (mg/g), respectively; K_1 is the rate constant of the PFO model for the adsorption process (1/min); K_2 is the rate constant for the PSO model (g/gmin); α is the initial sorption rate (mol/gmin); β is the desorption constant (g/mol); k_i is the IPD constant (mg/gmin$^{0.5}$); and C (mg/g) is the intercept that gives an idea about boundary layer thickness—the larger the intercept is equal to the greater value of boundary layer effect.

The results of kinetics of sorption study obtained after optimization of all parameters are shown in Figure 4. From adsorption-reaction models, PFO (Figure 4(a)), PSO (Figure 4(b)), and Elovich (Figure 4(c)) were tested. Depending on R^2 values, PSO model relatively fits well than PFO and Elovich and its theoretical equilibrium capacity values (10.41 mg/g) also fit well with the experimental data values (10.87 mg/g). But there is great variation between experimental (3.133 mg/g) and theoretical (10.41 mg/g) values for PFO. Often, the calculated q_e value is less than the experimental value, but it should be close to each other to say the model is fitted well [26].

The calculated results and different constants for kinetic model are presented in Table 3. From adsorption-diffusion model which helps to check whether the reaction mechanism is under control of adsorption-diffusion in addition to surface reaction, the intraparticle diffusion (IPD) model was tested. Being the R^2 values for IPD is relatively less than other adsorption-reaction models, which suggests that the mechanism is not under control of adsorption-diffusion kinetics; actually, to say the reaction is under the control of diffusion kinetics, the IPD linear line should pass through the origin (C = O), unlike that of obtained result in this paper. Therefore, it is possible to deduce that the reaction is totally under control of surface/adsorption-reaction [27].

3.8. Thermodynamics Study. The effect of temperature on lead ion sorption is shown in Figure 5(a). The values of ΔG^o being negative and the values of ΔH^o being positive indicate the respective spontaneous and an endothermic reaction of sorption (Table 4). As temperature increases, the ΔG^o values decrease, which shows that the sorption process of lead ion is high at high temperature. The thermodynamic parameters (ΔG, ΔH, and ΔS) can be calculated using the following equation:

$$\begin{aligned}
\Delta G &= -RT\ln K_c,\\
\ln K_c &= -\left(\frac{\Delta H^o}{RT}\right) + \frac{\Delta S^o}{R},\\
\Delta G^o &= \Delta H^o - T\Delta S^o,
\end{aligned} \tag{6}$$

where R (8.314 J/molK) is the universal gas constant, T is the absolute temperature, and K_c is the standard thermodynamic equilibrium constant defined by q_e/C_e. By plotting the graph of $\ln K_c$ versus $1/T$, the value of ΔH^o and ΔS^o can be estimated from the slopes and intercept values. The decrease in ΔG^o with increasing of temperature indicates more efficient sorption at higher temperature [28].

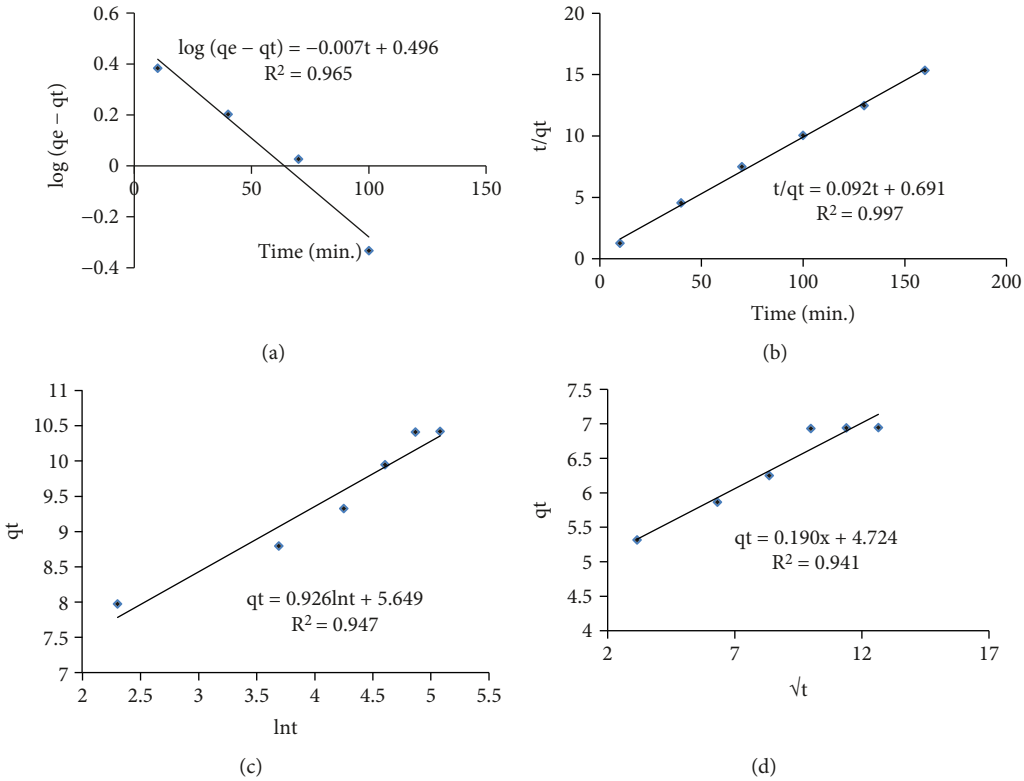

Figure 4: Plot of (a) pseudo-first order, (b) pseudo-second order, (c) Elovich, and (d) intraparticle diffusion model.

Table 3: Kinetic constants and coefficient values of lead sorption on binary metal oxides.

Metal	Pseudo-first				Pseudo-second			IPD		Elovich model			
	q_e *	K_1	q_e (mg/g)	R^2	K_2	q_e (mg/g)	R^2	k_{dif}	R^2	C	β	α	R^2
Pb(II)	10.41	0.016	3.133	0.965	0.012	10.87	0.997	0.19	0.947	4.72	1.08	173	0.941

*Represents calculated q_e values.

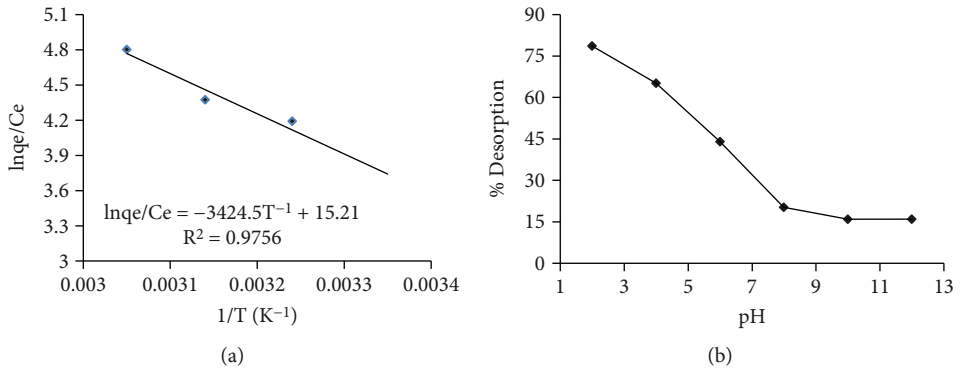

Figure 5: (a) Plot of thermodynamic study and (b) effect of pH on desorption of lead ion at various pH values.

3.9. Desorption Study. From the reproducibility/desorption studies (Figure 5(b)), as pH increases, the amount of desorption of lead ion decreases. About 79% of adsorbed lead ions were desorbed. Desorption efficiency was calculated using the equation as given below:

$$\%\ \text{desorption efficiency} = \frac{\text{desorbed}}{\text{adsorbed}} * 100, \quad (7)$$

where desorbed is the amount of the lead ion that was removed from the loaded powder after desorption study and adsorbed is $C_o - C_e$ for each recovery process.

4. Conclusion

TiO_2-Fe_2O_3 oxides nanocomposite containing different percentage of iron oxide was successfully synthesized using

Table 4: Values of thermodynamic parameters for lead ion sorption.

T (K)	ΔG (kJ/mol)	ΔH (kJ/mol)	ΔS (J/molK)
298	−9.219	28.471.3	126.48
308	−10.48		
318	−11.75		
328	−13.01		

impregnation method. The well impregnation of iron oxides on titanium oxides was confirmed by FTIR, XRD, and SEM-EDX (morphology-composition) analysis. FTIR and XRD analytical techniques confirm the appearance of crystalline binary metal oxide. The obtained approximate particle size for impregnated binary oxide was 31 nm. The superior stability of TiO_2-Fe_2O_3 oxide was revealed by TG-DTA analysis. Factors affecting sorption experiment (pH, adsorbent dose, speed of agitation, time of contact, and initial lead ion concentration) were optimized. Langmuir absorption isotherm fits well than other isotherms models. From PFO, FSO, Elovich, and adsorption-reaction kinetic models, PSO fits the adsorption mechanism well. The IPD adsorption-diffusion model fails to fit well, and its line did also not pass through the origin. Therefore, the adsorption kinetics is under control of adsorption-reaction mechanism. The assistance of temperature increment for adsorption of lead ion on the adsorbent and spontaneity of the reaction was proofed by thermodynamics study.

Data Availability

The [Excel] data used to support the findings of this study are available from the corresponding author upon request.

Conflicts of Interest

The authors declare that they have no conflicts of interest.

Authors' Contributions

The study and the first draft writing were conducted by Buzuayehu Abebe, and the supervision and edition were done by Dr. H C. Ananda Murthy. Both authors participated in drafting the manuscript.

Acknowledgments

The authors are grateful to the management of Adama Science and Technology University for providing the financial support towards this research work. The authors acknowledge Mr. Yilkal Dessie for the software support, Dr. Senthilkumar Subramanian for the characterization support, and Guta Amanu for his assistance in the laboratory.

References

[1] J. M. Rivera, S. Rincón, C. Ben Youssef, and A. Zepeda, "Highly efficient adsorption of aqueous Pb(II) with mesoporous metal-organic framework-5: an equilibrium and kinetic study," *Journal of Nanomaterials*, vol. 2016, 9 pages, 2016.

[2] D. Mehta, S. Mazumdar, and S. K. Singh, "Magnetic adsorbents for the treatment of water/wastewater—a review," *Journal of Water Process Engineering*, vol. 7, pp. 244–265, 2015.

[3] L. Durães, O. Oliveira, L. Benedini, B. F. O. Costa, A. Matos Beja, and A. Portugal, "Sol–gel synthesis of iron(III) oxyhydroxide nanostructured monoliths using $Fe(NO_3)_3{\cdot}9H_2O$/CH_3CH_2OH/NH_4OH ternary system," *Journal of Physics and Chemistry of Solids*, vol. 72, no. 6, pp. 678–684, 2011.

[4] I. J. Porter, S. K. Cushing, L. M. Carneiro et al., "Photoexcited small polaron formation in goethite (α-FeOOH) nanorods probed by transient extreme ultraviolet spectroscopy," *The Journal of Physical Chemistry Letters*, vol. 9, no. 14, pp. 4120–4124, 2018.

[5] Y. A. Gromova, V. G. Maslov, M. A. Baranov et al., "Magnetic and optical properties of isolated and aggregated $CoFe_2O_4$ superparamagnetic nanoparticles studied by MCD spectroscopy," *Journal of Physical Chemistry*, vol. 122, no. 21, pp. 11491–11497, 2018.

[6] K. Nguyen, N. D. Hoa, C. M. Hung, D. T. Thanh Le, N. Van Duy, and N. Van Hieu, "A comparative study on the electrochemical properties of nanoporous nickel oxide nanowires and nanosheets prepared by a hydrothermal method," *RSC Advances*, vol. 8, no. 35, pp. 19449–19455, 2018.

[7] X. Huang, G. Zhao, G. Wang, and J. T. S. Irvine, "Synthesis and applications of nanoporous perovskite metal oxides," *Chemical Science*, vol. 9, no. 15, pp. 3623–3637, 2018.

[8] M. Rostami, M. Aghajanzadeh, M. Zamani, H. K. Manjili, and H. Danafar, "Sono-chemical synthesis and characterization of Fe_3O_4@mTiO_2-GO nanocarriers for dual-targeted colon drug delivery," *Research on Chemical Intermediates*, vol. 44, no. 3, pp. 1889–1904, 2017.

[9] X.-F. Dong, H.-B. Zou, and W.-M. Lin, "Effect of preparation conditions of CuO–CeO_2–ZrO_2 catalyst on CO removal from hydrogen-rich gas," *International Journal of Hydrogen Energy*, vol. 31, no. 15, pp. 2337–2344, 2006.

[10] B. Abebe, A. M. Taddesse, T. Kebede, E. Teju, and I. Diaz, "Fe-Al-Mn ternary oxide nanosorbent: synthesis, characterization and phosphate sorption property," *Journal of Environmental Chemical Engineering*, vol. 5, no. 2, pp. 1330–1340, 2017.

[11] E. Katsou, S. Malamis, and K. J. Haralambous, "Industrial wastewater pre-treatment for heavy metal reduction by employing a sorbent-assisted ultrafiltration system," *Chemosphere*, vol. 82, no. 4, pp. 557–564, 2011.

[12] X. Tang, H. Zheng, H. Teng et al., "Chemical coagulation process for the removal of heavy metals from water: a review," *Desalination and Water Treatment*, vol. 57, no. 4, pp. 1733–1748, 2016.

[13] J. Ding, L. Wei, H. Huang et al., "Tertiary treatment of landfill leachate by an integrated electro-oxidation/electro-coagulation/electro-reduction process: performance and mechanism," *Journal of Hazardous Materials*, vol. 351, pp. 90–97, 2018.

[14] B. E. Monárrez-Cordero, P. Amézaga-Madrid, A. Sáenz-Trevizo, P. Pizá-Ruiz, W. Antúnez-Flores, and M. Miki-Yoshida, "Synthesis and characterization of composite Fe-Ti oxides nanoparticles with high surface area obtained via AACVD," *Ceramics International*, vol. 44, no. 6, pp. 6990–6996, 2018.

[15] S. Malamis, E. Katsou, M. Stylianou, K. J. Haralambous, and M. Loizidou, "Copper removal from sludge permeate with ultrafiltration membranes using zeolite, bentonite and

vermiculite as adsorbents," *Water Science and Technology*, vol. 61, no. 3, pp. 581–589, 2010.

[16] R. Saravanan, J. Aviles, F. Gracia, E. Mosquera, and V. K. Gupta, "Crystallinity and lowering band gap induced visible light photocatalytic activity of TiO_2/CS (Chitosan) nanocomposites," *International Journal of Biological Macromolecules*, vol. 109, pp. 1239–1245, 2018.

[17] Y. Wang, L. Li, X. Huang, Q. Li, and G. Li, "New insights into fluorinated TiO_2 (brookite, anatase and rutile) nanoparticles as efficient photocatalytic redox catalysts," *RSC Advances*, vol. 5, no. 43, pp. 34302–34313, 2015.

[18] A. S. Zhao, S. Zhou, Y. Wang, J. Chen, C. R. Ye, and N. Huang, "Molecular interaction of fibrinogen with thermally modified titanium dioxide nanoparticles," *RSC Advances*, vol. 4, no. 76, pp. 40428–40434, 2014.

[19] N. A. Jamalluddin and A. Z. Abdullah, "Reactive dye degradation by combined Fe(III)/TiO_2 catalyst and ultrasonic irradiation: effect of Fe(III) loading and calcination temperature," *Ultrasonics Sonochemistry*, vol. 18, no. 2, pp. 669–678, 2011.

[20] M. A. Ahmed, E. E. El-Katori, and Z. H. Gharni, "Photocatalytic degradation of methylene blue dye using Fe_2O_3/TiO_2 nanoparticles prepared by sol–gel method," *Journal of Alloys and Compounds*, vol. 553, pp. 19–29, 2013.

[21] N. Abbas, G. N. Shao, M. S. Haider, S. M. Imran, S. S. Park, and H. T. Kim, "Sol–gel synthesis of TiO_2-Fe_2O_3 systems: effects of Fe_2O_3 content and their photocatalytic properties," *Journal of Industrial and Engineering Chemistry*, vol. 39, pp. 112–120, 2016.

[22] W. Subramonian, T. Y. Wu, and S.-P. Chai, "Photocatalytic degradation of industrial pulp and paper mill effluent using synthesized magnetic Fe_2O_3-TiO_2: treatment efficiency and characterizations of reused photocatalyst," *Journal of Environmental Management*, vol. 187, pp. 298–310, 2017.

[23] N. M. Al-Hada, E. Saion, H. M. Kamari et al., "Structural, morphological and optical behaviour of PVP capped binary $(ZnO)_{0.4}$ $(CdO)_{0.6}$ nanoparticles synthesised by a facile thermal route," *Materials Science in Semiconductor Processing*, vol. 53, pp. 56–65, 2016.

[24] A. E. Ofomaja, E. I. Unuabonah, and N. A. Oladoja, "Competitive modeling for the biosorptive removal of copper and lead ions from aqueous solution by Mansonia wood sawdust," *Bioresource Technology*, vol. 101, no. 11, pp. 3844–3852, 2010.

[25] Y. Liu, C. Luo, J. Sun, H. Li, Z. Sun, and S. Yan, "Enhanced adsorption removal of methyl orange from aqueous solution by nanostructured proton-containing δ-MnO_2," *Journal of Materials Chemistry A*, vol. 3, no. 10, pp. 5674–5682, 2015.

[26] K. L. Tan and B. H. Hameed, "Insight into the adsorption kinetics models for the removal of contaminants from aqueous solutions," *Journal of the Taiwan Institute of Chemical Engineers*, vol. 74, pp. 25–48, 2017.

[27] H. Yang, S. Masse, M. Rouelle et al., "Magnetically recoverable iron oxide–hydroxyapatite nanocomposites for lead removal," *International journal of Environmental Science and Technology*, vol. 12, no. 4, pp. 1173–1182, 2015.

[28] R. Alfaro-Cuevas-Villanueva, A. R. Hidalgo-Vazquez, C. D. J. Cortes Penagos, and R. Cortes-Martinez, "Thermodynamic, kinetic, and equilibrium parameters for the removal of lead and cadmium from aqueous solutions with calcium alginate beads," *The Scientific World Journal*, vol. 2014, 9 pages, 2014.